



Nanodiamond-decorated ZnO catalysts with enhanced photocorrosion-resistance for photocatalytic degradation of gaseous toluene

Juan Liu¹, Penglu Wang¹, Wenqiang Qu, Hongrui Li, Liyi Shi, Dongsong Zhang*

Department of Chemistry, College of Sciences, Research Center of Nano Science and Technology, School of Materials Science and Engineering, Shanghai University, Shanghai, 200444, China

ARTICLE INFO

Keywords:

Photocatalytic degradation
Toluene
Photocatalysis
Volatile organic compounds

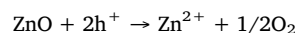
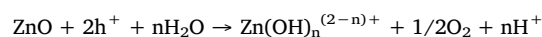
ABSTRACT

Photocatalytic degradation of indoor volatile organic compounds (VOCs) is considered as one of a promising strategy for resolving indoor pollution problems. Zinc oxide has been widely used in photocatalysis. However, the photocorrosion of ZnO restrains its further application. Herein, we decorated ZnO with nanodiamonds to solve the photocorrosion problem of ZnO for photocatalytic degradation of gaseous toluene. The photocorrosion-resistance of nanodiamond-decorated ZnO catalysts was enhanced. It was demonstrated that after the decoration of nanodiamonds, the optical absorption and transient photocurrent were effectively increased, while the photoluminescence intensity and electrochemical impedance were greatly reduced, indicating that nanodiamonds decoration not only improved the light adsorption for ZnO, but also promoted the charge transfer and eventually enhanced the photocatalytic oxidation efficiency of toluene. We hope that this work could propose possible ways to relieve the photocorrosion of ZnO semiconductor in the photocatalytic application and provide new insights into the degradation of gaseous pollutants.

1. Introduction

In recent years, the elimination of indoor volatile organic compounds (VOCs) has attracted significant attention. Indoor VOCs including benzene, toluene, formaldehyde, xylene, styrene, trichlorethylene, chloroform and so on [1], can influence kidney and liver function of human beings or even cause cancer [2]. In order to solve the problem of indoor air pollution, many approaches had been developed to eliminate indoor VOCs, e.g., physical adsorption [3], thermocatalytic oxidation [4], plasma technology [5], and photocatalytic elimination [6–8]. As a green technology, photocatalytic elimination had been increasingly used to degrade VOCs for the past few years. Therefore, photocatalytic materials including conventional titanium dioxide [9,10], zinc oxide [11], cadmium sulfide [12], cerium oxide [13], carbon nitride [14–16], perovskite [17], organic semiconductor [18] and Bi-based photocatalyst [19–21] had gradually attracted great attentions. Among them, TiO₂ had been extensively studied due to its good chemical stability, thermal stability, high efficiency and non-toxicity [22–24]. Different from TiO₂, although ZnO is also a typical n-type semiconductor and often used in some fields of photocatalysis, it is rarely used for the photocatalytic elimination of gaseous pollutants. It had been reported that Kant et al. [25] fabricated α-Fe₂O₃/Au/ZnO

heterostructure thin films and used it as photoanode for photoelectrochemical water splitting. Theoretically, the energy gap of ZnO at room temperature is 3.38 eV, which is similar to 3.2 eV of anatase TiO₂ and always shows similar photocatalytic efficiency in the initial stages of photocatalytic reaction with TiO₂. However, the photocorrosion of ZnO is a common and serious phenomenon that always occurs in the long-term photocatalytic process and extremely inhibits its further application. The collapse of the ZnO structure may occur after UV irradiation through the following self-oxidation reaction [26,27]:



where h⁺ represents the positive hole generated by UV irradiation. Several strategies had been employed to inhibit the photocorrosion of ZnO, such as combination with another semiconductor, deposition of noble metals and so on. Ma et al. [28] found that loading Ag on ZnO could relieve the photocorrosion and enhance the photocatalytic stability in MB solution. Yu et al. [29] synthesized a “core-shell” structure catalyst that with hollow ZnO as core and ZnS as shell, which could conquer the photocorrosion compared with ZnO. At the same time, to improve the photocatalytic activity, many research groups had reported

* Corresponding author.

E-mail address: dszhang@shu.edu.cn (D. Zhang).

¹ These authors contributed equally to this work.

ZnO based heterojunction photocatalytic materials, such as $\text{Cu}_2\text{ZnSnS}_4/\text{ZnO}$ [30], $\text{ZnO}/\text{ZnS}/\text{g-C}_3\text{N}_4$ [31], and nickel zinc ferrite nanoparticles/ ZnO [32]. However, it was still a challenge to solve the photocorrosion problem of ZnO for photocatalytic degradation of VOCs.

The nanodiamond (ND) owns a unique crystalline phase that composed of a sp^2 hybrid graphitic carbon shell and a sp^3 hybrid carbon diamond core [33], which determines that ND possesses unique physical and chemical properties and more potential than traditional carbon materials in photocatalytic reaction. Kim et al. [34] had investigated the photocatalytic decomposition of toluene using ND-supported TiO_2 catalysts. It was found that ND promoted the complete photooxidation of toluene on TiO_2 and TiO_2/ND was more tolerant towards photocorrosion than bare TiO_2 , which was mainly because that the addition of ND surface facilitated entire oxidation of toluene on TiO_2 and reduced the deactivation of TiO_2 with time prolonged. Moreover, the ND is comparable in some properties to noble metal Pt, but it is much cheaper than Pt. Therefore, the ND had been selected to improve the photocatalytic activity and relieve the photocorrosion of ZnO in the photocatalytic oxidation of toluene. As the ND had been reported that the surface functional groups of ND would obviously affect the photoactivity of TiO_2 [34], the ND was modified in various methods [35] including graphitization, oxidation, and acid treatment, mainly aiming to study the effect of thick surface graphitic layer of ND, elimination of surface graphitic carbon shell of ND, and oxygen containing functionalities of ND on the photocatalytic performance.

In this work, ND-decorated ZnO heterojunction photocatalysts were prepared for photocatalytic oxidation of toluene under UV-365 illumination. To evaluate the effect of ZnO crystal faces on the performance, we prepared four types of ZnO with different exposed crystal faces to compare the difference in the activity. The photocorrosion-resistance of the optimized ND-decorated ZnO catalysts and bare ZnO were evaluated and compared by carrying out five reaction cycles of photocatalytic oxidation of toluene under UV-365 illumination. The XRD, HR-TEM, XPS, FTIR were carried out to confirm the successful configuration of ZnO/ND heterojunction. The Raman spectra, optical absorption, photoluminescence, transient photocurrent response, electrochemical impedance spectra, Mott-Schottky spectra, electron paramagnetic resonance and *in situ* DRIFTS were all conducted to investigate the promotion mechanism of ND decoration and the enhanced photocorrosion-resistance of ZnO catalysts.

2. Experimental

2.1. Catalysts preparation

All the chemicals were analytical grade and purchased from Sinopharm Chemical Reagent Co., Ltd. (China) without further purification. Pure nanodiamond (ca. 10 nm diameter) was purchased from Kesiman Grinding Technology Co. Ltd. (Guangzhou, China), and the treatment methods were described in the Supplementary Data.

The ND-decorated ZnO samples were synthesized via a simple dehydration condensation process between the hydroxyl groups on the surface of ZnO and the oxygen-containing functional groups on ND [35]. 10 mg ND was first added to deionized water separately and ultrasonicated for 30 min. Then 100 mg ZnO powder was added into the above suspension and stirred for 30 min and aged for 12 h followed by filtration. The obtained gray powder was dried at 70 °C for 12 h and the obtained sample was labelled as ZnO-X/ND (where X = I, II, III represent different morphologies, see Supplementary Information for details).

2.2. Photocatalytic toluene degradation measurements

The photocatalytic degradation of toluene was carried out in a closed-circulation reactor at ambient environment [23]. The volume of stainless-steel reactor is approximately 290 ml. The reactor and a gas

chromatograph (GC 9890B equipped with a flame ionization detector and methane reforming furnace) were connected by a stainless-steel tube with 2 mm radius. A full-band xenon lamp (50 W) with Band-Pass UV-365 filter was used as a lighting source. Prior to each experiment, 0.1 g photocatalyst powder was uniformly dispersed in water and then coated on a round glass plate with a diameter of 5 cm, subsequently exposed to xenon lamp for one hour to remove any organics that might be adsorbed. After that, the standard gas (50 ppm toluene in air) was passed into the reactor until the toluene concentration in the reactor no longer changed and stabilized at about 50 ppm.

2.3. Catalyst characterization

The morphology was characterized by field emission scanning electron microscopy (FESEM, JSM-7500F, JEOL LTD., Japan) and the high-resolution transmission electron microscopy (HR-TEM, JEM-2100F, JEOL LTD., Japan). The elemental distribution was characterized by energy dispersive spectrometer (EDS). The crystal structure was performed by using a Rigaku D/MAS-RB X-ray diffractometer with $\text{Cu K}\alpha$ radiation at a scanning step of 8° min^{-1} (XRD, D/MAS-RB, Rigaku, Japan). The intrinsic structure was obtained by using Raman spectrometer with the laser at 325 nm and 532 nm as the excitation source (Raman, LabRAM HR Evolution, Horiba, France). The surface electronic states were analyzed by X-ray photoelectron spectroscopy (XPS, Axis Ultra Dld, Shimadzu, Japan). The surface functional groups of ND were analyzed by Fourier transform infrared spectroscopy using an AVATAR370 Fourier transform infrared spectrometer (FTIR, AVATAR370, Thermo Nicolet Corporation, American). The UV-vis absorbance of samples was recorded by diffuse reflectance spectra (DRS) using UV-vis spectrophotometer (UV-vis absorbance, UV-2600, Shimadzu, Japan). Fluorescence intensity of samples was measured by photoluminescence spectra using fluorescence spectrometer with a continuous wave laser (maximum power 800 mW) as the excitation light (PL, FS-5, Edinburgh). The transient photocurrent responses, electrochemical impedance spectra (EIS) and Mott-Schottky spectra were measured in a quartz cell with a conventional three-electrode system on an electrochemical workstation (CHI660E, CHENHUA Instrument Company). The electron paramagnetic resonance characterization (EPR, EMX-8/2.7, Bruker, American) was carried out at room temperature with spin-trapped paramagnetic species with 5,5-dimethyl-1-pyrroline *N*-oxide (DMPO) as radical scavenger. The toluene temperature-programmed desorption (Toluene-TPD) was tested on a Tianjin XQTP-5080 autoadsorption apparatus. Before test, 50 mg sample was pretreated at room temperature in high purity (99.999%) N_2 (30 mL min^{-1}) for 30 min. *In situ* DRIFTS experiments were carried out by using Bruker Tensor 27 FTIR spectrometers [36]. Catalysts were pretreated under Helium (30 mL min^{-1}) for 1 h at room temperature to remove adsorbed impurities. After recording the background spectrum with Helium flow and subtracting the background spectrum, the samples were exposed to 50 ppm gaseous toluene with 50% oxygen. The DRIFTS spectra of samples were recorded by accumulating 32 scans with a resolution of 4 cm^{-1} at a given interval at room temperature.

3. Results and discussion

3.1. Photocatalytic degradation of toluene

For purpose of comparing the photocatalytic activity of ZnO and ZnO/ND catalysts, the photocatalytic degradation of gaseous toluene had been performed (Fig. 1(a)). Firstly, no obvious reduction in toluene content or increase in CO_2 content were observed in the blank control experiments without either the photocatalyst or UV light illumination (Fig. S1). From Fig. 1(a), it was clear that after the modification ND, the toluene oxidation efficiency was improved, indicating that the effective heterogeneous combination between ZnO and ND. In the case of ZnO/ND, the 50 ppm toluene degradation activity decreased by 100%

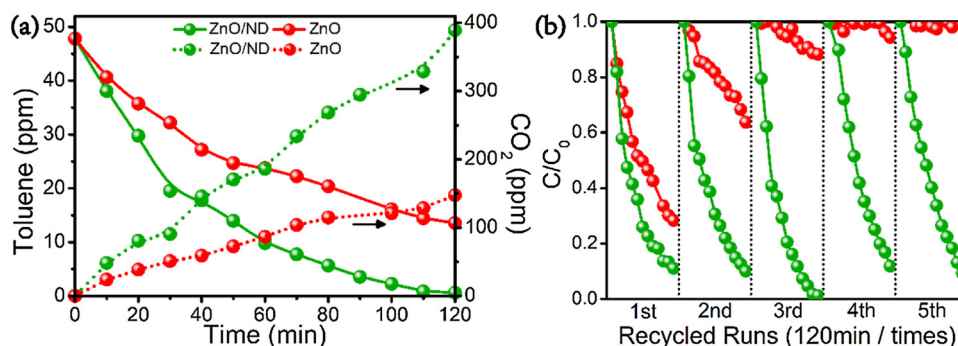


Fig. 1. (a) Photocatalytic degradation of gaseous toluene and the CO₂ yield of ZnO and ZnO/ND catalysts; (b) Stability after cycles: red lines represented ZnO and green lines represented ZnO/ND (For interpretation of the references to colour in this figure legend, the reader is referred to the web version of this article).

within 120 min. Fig. 1(a) also showed that the trend of CO₂ generation corresponded to that of toluene degradation. The mineralization capacity of ZnO/ND was obviously higher than that of ZnO. However, the amount of CO₂ was slightly higher than the theoretical value, which might be due to the fact that a small amount of toluene adsorbed on the surface of photocatalysts were also been photodegraded thus led to forming more CO₂.

Furthermore, since the performance of ZnO was affected by factors such as morphology and crystal plane, ND decorated ZnO with different morphologies were also compared. It could be seen that the photocatalytic activities of photocatalysts gradually decreased in the order of ZnO, ZnO-III, ZnO-I and ZnO-II (Fig. S2(a) and (b)). The morphology of as prepared ZnO-I, ZnO-II, ZnO-III and ZnO-IV photocatalysts were studied and shown in Fig. S3. It could be seen that ZnO was a microsphere composed of many thin sheets with an inhomogeneous color (Fig. S3(a)), ZnO-I was rod-like (Fig. S3(b)) and ZnO-II like a thick needle (Fig. S3(c)). The star-like morphology of ZnO-III could be seen in Fig. S3(d). Besides, it had been reported that the ZnO owned the highest proportion of (0001) crystal plane and ZnO-II with most (100) crystal plane exposed [37]. Thus, the photocatalytic efficiency of toluene degradation for ND decorated ZnO with different morphologies demonstrated that the (0001) crystal plane lead to a higher photocatalytic activity, whereas the (100) plane showed negative effects.

As the introduction of surface functional groups on the ND particles played an important role in the photocatalytic activity, ZnO/G-ND, ZnO/O-ND and ZnO/A-ND were tested for the degradation of toluene to study the influence of different modifications of ND for photocatalytic performance (Fig. S2(c) and (d)). After the graphitization under high-temperature, the photocatalytic activity of ZnO/G-ND (graphitized ND) was declined, which was might be ascribed to the aggregation of ND particles under high-temperature, the addition of graphitic sp²-carbon shell and the lack of oxygen-containing surface functionality, making the weaker connection of ZnO and G-ND. For the oxidized ND, the photocatalytic activity of ZnO/O-ND was also reduced, indicating the elimination of surface graphitic carbon shell led to the reduction of conductivity on the ND surface. After acid-treatment, the conductivity of ND surface was also reduced due to a number of oxygen-containing functional groups, and ND was more likely to agglomerate into large particles, that was why it had the lowest photocatalytic activity. From the above results, it was obvious to see that the thick surface graphitic layer of ND resulting from graphitization, the removal of surface graphitic carbon layer of ND by oxidation, and the presence of oxygen containing functionalities of ND caused by acid treatment were all not beneficial to the photocatalytic performance. In final, ZnO/ND catalyst exhibited the best performance and the bare nanodiamond showed better synergistic effect with ZnO to perform enhanced photocatalytic activity of toluene removal.

To investigate and compare the photocorrosion-resistance of the optimal ZnO/ND and bare ZnO catalyst, five successive experimental cycles were performed to study the photodegradation performance of

toluene. As shown in Fig. 1(b), the stability of ZnO decreased with increasing number of cycles, while that of ZnO/ND barely changed after five reaction cycles under the same condition. Since the initial toluene gas concentration in the reactor was not exactly the same at the beginning of each cycle (Fig. S4(a)). In fact, the total amount of toluene degradation in the 3rd cycle was not the largest, but because of its low initial concentration, the degradation efficiency seemed to be higher than others after being converted to C/C₀. The five cycled stability results were also shown with the variation of toluene concentration as the function of cycled runs in Fig. S4(a). Furthermore, in order to eliminate the effect of initial photocatalytic activity on stability, we determined the degradation of toluene in cycle 1st as ΔC_1 , and then divided the degradation of toluene per cycle (ΔC) by ΔC_1 (Fig. S4(b)). Thus, the differentiated photocatalytic activity of ZnO and ZnO/ND would be normalized and the photo-stability could be clearly compared by the change of $\Delta C/\Delta C_1$, which was the degree of toluene degradation for each cycle without the influence of the higher photocatalytic activity of ZnO/ND. It was easy to figure out that the improved photocatalytic activity of ZnO/ND was not the reason for its good stability and ZnO/ND indeed showed superior photocatalytic stability than bare ZnO.

3.2. The morphology and structure investigation

To provide more direct evidence for the exposed planes of ZnO, ZnO-I, ZnO-II and ZnO-III, we recorded the XRD spectra (Fig. S5) of the as-mentioned samples. The diffraction peaks with 2θ at 31.8, 34.4, 36.3, 47.5, 56.6, 62.9, 66.4, 68.0, 69.1, 72.6 and 77.0° could be assigned to (100), (002), (101), (102), (110), (103), (200), (112), (201), (004) and (202) facets of zincite ZnO, respectively. It could be clearly seen that the peak intensities of different samples are different from each other due to the different exposed planes. The surface information of nanodiamonds modified in various ways could be seen in FTIR (Fig. S6). FTIR spectra of bare ND, G-ND, A-ND and O-ND showed clear differences and bands at around 1627, 1780, 3440 cm⁻¹ were found for almost all the samples. The sharp peak at ~1627 cm⁻¹ was assigned to the C=C stretching vibration originating from sp² hybridized carbon or the O-H [38]. The peak at ~1780 cm⁻¹ was caused by the C=O stretching vibration. Broad absorption of associated hydroxyl groups was generated at ~3440 cm⁻¹ for the oxidized ND [39]. After high-temperature calcination, the absorption bands in the range of 1600–2000 cm⁻¹ of graphitized ND almost vanished and the band at ~1560 cm⁻¹ could be assigned to the C–C stretching vibrations of aromatic C=C, indicating the nanodiamond had been successfully graphitized through high-temperature calcination. After oxidation, the C=O and O–H stretching vibration became much stronger because of the formation of more oxygen-containing surface functional groups. As for the acidified ND, the C=O stretching vibration slightly increased, indicating that the strong acid treatment could also introduce some oxygen-containing groups.

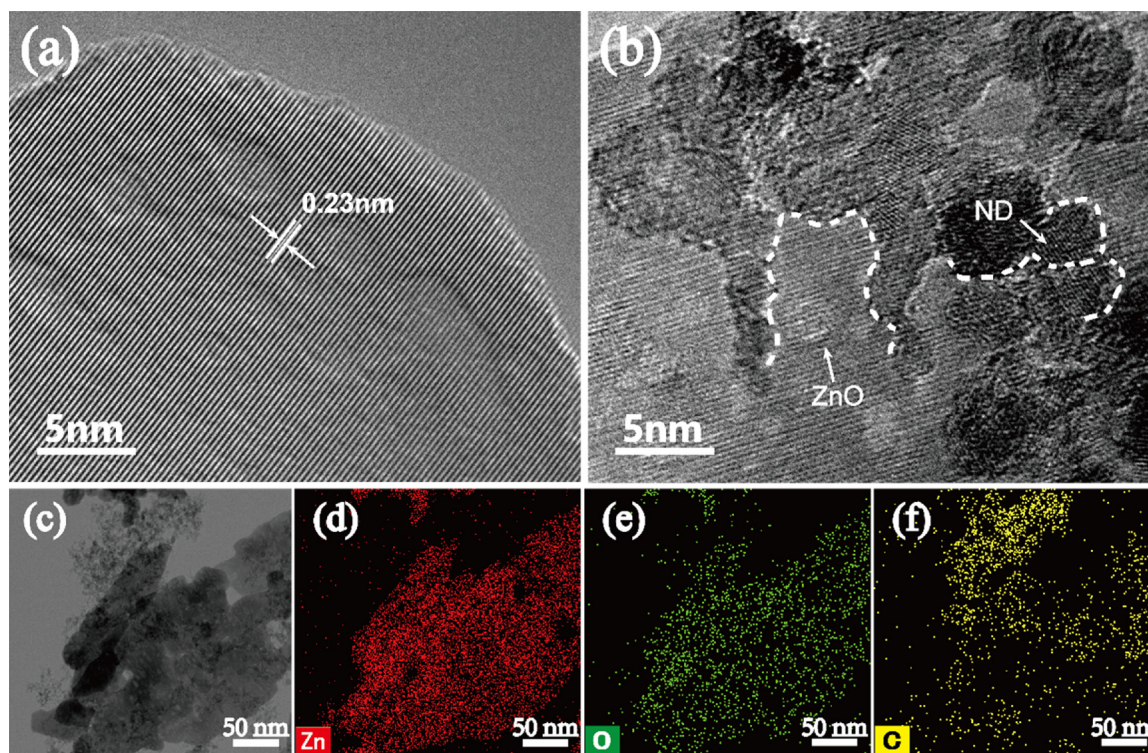


Fig. 2. HRTEM images of (a) ZnO and (b) ZnO/ND; (c) high angle annular dark-field (HAADF) image of ZnO/ND; EDS elemental mapping of (d) Zn, (e) O and (f) C for ZnO/ND.

Fig. 2 showed the HR-TEM images of ZnO and the EDS mapping of ZnO/ND. The lattice spacing observed in ZnO was $\sim 2.3 \text{ \AA}$, which corresponded to the (0001) crystallographic plane of ZnO (see Fig. 2(a)) [40]. Fig. 2(b) showed that the surface of ZnO/ND was considerably covered by ND nanoparticles. The EDS mapping analysis of ZnO/ND was carried out to demonstrate the presence of ND on the surface of ZnO and C elemental spots were uniformly scattered on the surface of ZnO, confirming that the ND was well dispersed on the surface of ZnO.

Fig. 3 displayed the XRD pattern of ZnO/ND and ZnO catalysts before and after the photocatalytic reaction. It was easy to obtain that the XRD reflections of ZnO/ND was almost the same with that of ZnO, and no typical diffraction peaks of ND had been detected before reaction, indicating that the ND particle size was small and well dispersed on the surface of ZnO. After the reaction, since the peak intensity of ZnO was slightly decreased, the (111) facet characteristic peak of ND at 43.9° was revealed. In addition, XRD analyses clearly confirmed that the crystalline structure of ZnO/ND did not change significantly during

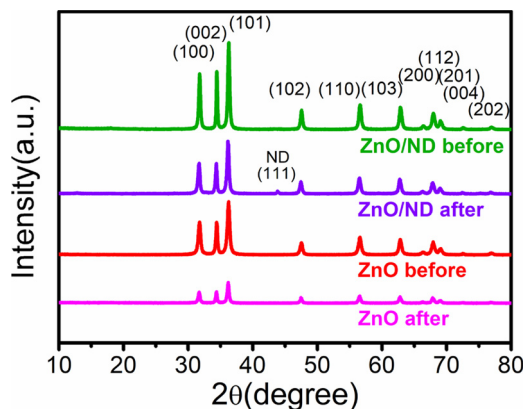


Fig. 3. XRD patterns of ZnO/ND and ZnO catalysts before and after five reaction cycles.

the photocatalytic reaction, but the peak intensity of ZnO was significantly weakened, which may be caused by the photocorrosion.

To further confirm the intrinsic crystal structure of ZnO and ZnO/ND catalysts and also those after five reaction cycles reaction, Raman spectra was obtained and shown in Fig. 4. When a laser at 325 nm as the excitation source (Fig. 4(a)), it was easy to see that all the catalysts presented typical crystal structure of ZnO, with bands generated at 572, 1146, 1726 cm^{-1} corresponding to the 1LO, 2LO, 3LO modes of hexagonal wurtzite crystal structure ZnO, respectively [41]. After decoration of ND, the peaks had no obvious change except that the intensity decreased a little bit, which was might because of the coverage of ND on the surface of ZnO. Meanwhile, the ZnO/ND catalyst after five reaction cycles still maintained the same structure of that before reaction, indicating no obvious collapse of ZnO observed. However, the crystallinity of ZnO declined a lot and Raman shift showed a red shift, which meant that serious photocorrosion may occur on ZnO and accorded well with the results of XRD. When we changed the laser to 532 nm, more refined structure of Zn species could be observed and shown in Fig. 4(b). As the carbon materials would show obvious fluorescence effect under 532 nm laser beam, only ZnO before and after reaction were studied herein. The peaks at 326, 380, 437, 582, 1073, 1150 cm^{-1} were assigned to E2(high)-E2, A1T, E2(high), E1L and 2LO modes of hexagonal wurtzite crystal structure ZnO, respectively [41]. After reaction, the wavenumbers shifted from 326 to 332 cm^{-1} , 1073 to 1095 cm^{-1} , indicating the structure of ZnO was changed somewhat. In addition, there was a new peak at 390 cm^{-1} appearing, which was verified to be the $[\text{Zn}(\text{OH}_2)_6]^{2+}$ species [42], providing an solid evidence of the photocorrosion of ZnO by photo-generated holes.

3.3. Photo- and electro-chemistry performance

Optical absorption performance of ZnO and ZnO/ND was tested by UV-vis diffuse reflectance spectrum (DRS) and shown in Fig. 5(a). The onset absorption of them was determined at 380 nm and the absorption edge occurred at about 400 nm. In comparison with the pristine ZnO,

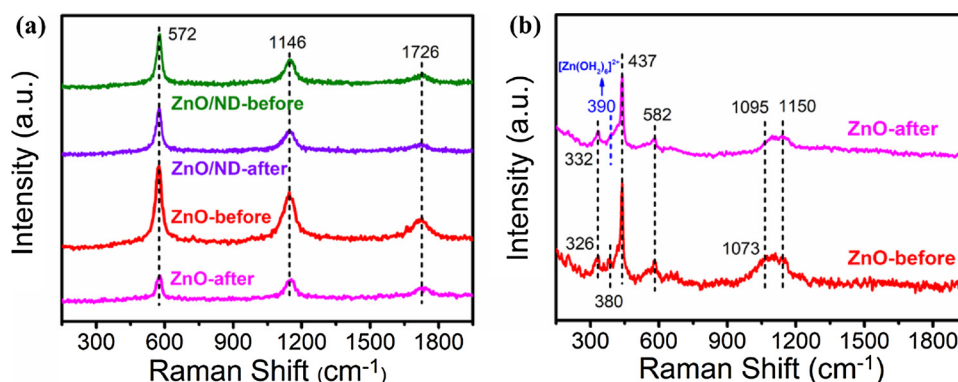


Fig. 4. Raman spectra with laser at (a) 325 nm and (b) 532 nm as excitation source for ZnO/ND and ZnO catalysts before and after five reaction cycles.

the absorption of ZnO/ND had been effectively improved. The inset figure of Tauc plot in Fig. 5(a) indicated that the bandgap of ZnO had been slightly narrowed by ND decoration, which well accorded with the enhanced optical absorption property of ZnO. In order to check the band gap of ND used in this work, the UV-vis diffuse reflectance spectrum of ND and the band gap calculated therefrom were shown in Fig. S7. It should be easy to find that the band gap of ND utilized herein was estimated to be 1.96 eV, which was much narrower than the bulk ND material (5.4 eV) and enabled the ND to adsorb UV light. Referred to some literatures, it could be concluded that the nanodiamond owns a unique crystalline phase that composed of a sp^2 hybrid graphitic carbon shell and a sp^3 hybrid carbon diamond core. Its unique structural characteristics make the band gap of nanodiamonds much smaller than that of bulk diamond [33].

The room temperature photoluminescence (PL) emission spectrum of ZnO and ZnO/ND was examined and shown in Fig. 5(b). The excited wavelength was 320 nm. The intensity of PL emission peak is related to the recombination probability of photoexcited charge carriers positively. There was a strong green emission band peaking around 544 nm and prior researches indicated that the green emission corresponded to the individual ionized oxygen vacancy [43]. The broad band arose due to the recombination of photogenerated hole with electron existing on the oxygen vacancy [44,45]. It was therefore reasonable to believe that the recombination of photogenerated electron-hole pairs on the surface of ZnO was suppressed effectively by loading ND, indicating that the effective separation of photo-generated electron-hole pairs indeed promoted the toluene oxidation efficiency for ND-decorated ZnO catalysts.

The transient photocurrent had been considered as the most efficient method to estimate the photocatalytic performance of composite photocatalyst [46]. As shown in Fig. 6(a), the electrode-type photocurrent profiles were obtained from the catalyst-coated electrode.

Compared to ZnO, the photocurrent response of ZnO/ND was effectively improved. In addition, the boosted charge transport could be verified by the reduced hemicycle radius electrochemical impedance spectra (EIS, Fig. 6(b)), which reflected the electric resistance of ZnO/ND was slower and confirmed the faster charge transfer ability of ZnO/ND heterojunction.

3.4. Surface elements and adsorption performance

To study the surface chemical composition of the samples, ZnO and ZnO/ND were further studied by XPS (Fig. 7(a–c)). All the XPS spectra were calibrated using C 1s standard peak located at 284.6 eV as a reference. Fig. 7(a) showed the survey spectra of ZnO and ZnO/ND, the element Zn and O in both catalysts can be seen. By comparing the O 1s peaks of ZnO and ZnO/ND in Fig. 7(b), it was found that the characteristic peak of O 1s shifted from 530.6 eV in ZnO to a higher binding energy of 532.1 eV in ZnO/ND, which was attributed to the formation of a heterojunction, resulting from the decrease of electron density around oxygen atoms [47]. Fig. 7(c) showed the Zn 2p spectrum with two peaks, the peaks at 1022.6 eV and 1045.8 eV were assigned to Zn 2p_{3/2} and 2p_{1/2} states, respectively, showing a normal state of Zn²⁺ in the sample [48,49].

Fig. 7(d) showed the FTIR spectrum of ZnO/ND. The broad absorption band at ~ 3428 cm⁻¹ was related to hydrogen bonded O–H stretching vibrations; peaks at ~ 2960 and ~ 2896 cm⁻¹ were corresponding to the C–H stretching vibration; peaks at ~ 1593 and ~ 1405 cm⁻¹ were assigned to O–C–O asymmetric and symmetric vibrations; the peaks at ~ 1090 cm⁻¹ was related to the C–O bonds; and the absorption bands at 400–600 cm⁻¹ were attributed to the stretching vibrations of Zn–O [50]. FTIR results demonstrated that the ND was well decorated on the ZnO surface.

The adsorption capacity toward toluene of catalysts had been

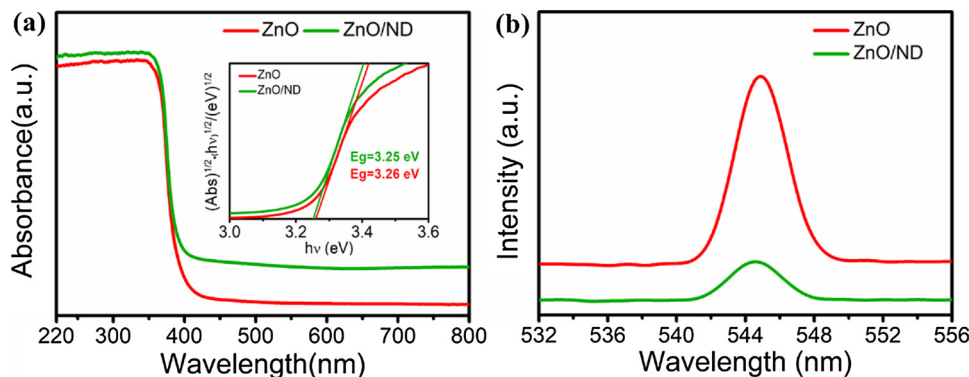


Fig. 5. (a) UV-vis diffuse reflectance spectra and calculated Tauc plot (inset) of ZnO and ZnO/ND catalysts; (b) The room temperature photoluminescence emission spectra of ZnO and ZnO/ND catalysts.

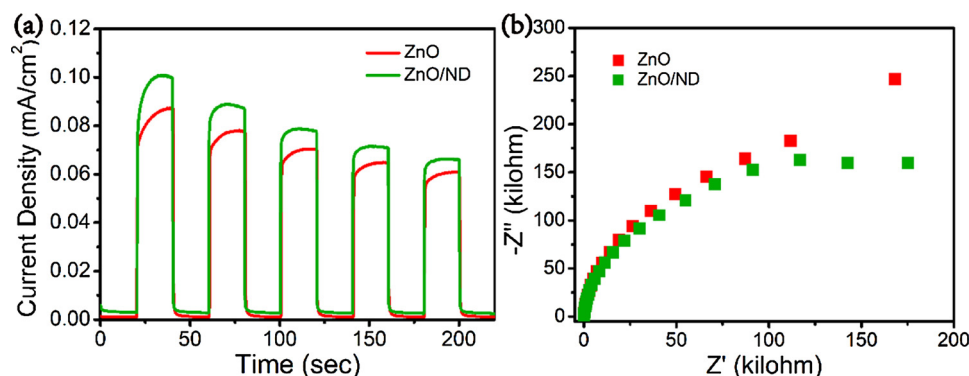


Fig. 6. (a) Transient photocurrent response curves and (b) electrochemical impedance spectra of ZnO and ZnO/ND catalysts.

investigated with the utilization of temperature-programmed desorption (TPD) technique (Fig. S8). As shown in the figure, ZnO/ND had the capacity to adsorb toluene, but ZnO almost showed no toluene adsorption in the testing temperature range, revealing that the ND decorated on the ZnO improved the adsorption of toluene on the surface and the toluene adsorption ability may be one of the main reasons for determining the catalytic performance of catalysts.

3.5. Discussion on reactive species

To further explore the possible reaction mechanism that beneficial for in-depth understanding the enhancement in the photocatalytic performance, electron paramagnetic resonance (EPR) were conducted to confirm the radicals generated in the reaction and the results were presented in Fig. 8. The previous work reported that the radical species of $\cdot\text{OH}$ and $\cdot\text{O}_2^-$ always took important roles in photocatalytic process [51]. In Fig. 8(a), no signal could be detected when the system was in dark. Under UV-365 light illumination, there were four characteristic peaks of the DMPO- $\cdot\text{O}_2^-$ adducts could be observed obviously, which demonstrated the $\cdot\text{O}_2^-$ had been formed through the reduction of O_2 .

Comparing ZnO and ZnO/ND, the signals collected from ZnO/ND were slightly stronger than that of ZnO. However, in Fig. 8(b), there were no signal of the $\cdot\text{OH}$ radical both in dark and under illumination. It meant that the h^+ generated from ZnO and ZnO/ND under the UV-365 light illumination could not oxidize the water molecular into $\cdot\text{OH}$ [52]. As the photocorrosion of ZnO had been successfully improved that shown in Fig. 1(b), the photo-generated h^+ might participated in the toluene oxidation reaction directly [36,53].

The Mott-Schottky plots of ND, ZnO and ZnO/ND were used to determine their flatband potential (V_{fb}), and Tauc plots shown in Figs. 5(a) and S7 were used to calculate their “band gaps”. The flat-band potential of ND, ZnO and ZnO/ND were *ca.* -0.91 V , -0.76 , -0.79 V vs. NHE, respectively (Fig. 9). When used as the standard, the lowest conduction band (CB) potential of ZnO and ND was -0.76 and -0.91 V , respectively [54]. The band gaps for as-prepared ZnO and ND was estimated to be 3.26 eV and 1.96 eV , respectively. Based on the Mott-Schottky plots and Tauc plots, the CB/VB energies were confirmed to be $-0.76/+2.50\text{ V}$ (for ZnO), $-0.91/+1.05\text{ V}$ (for ND) vs. NHE, respectively. The CB energy of ZnO was decreased to -0.79 V after ND modification, which was might because that the flat band of ZnO/ND

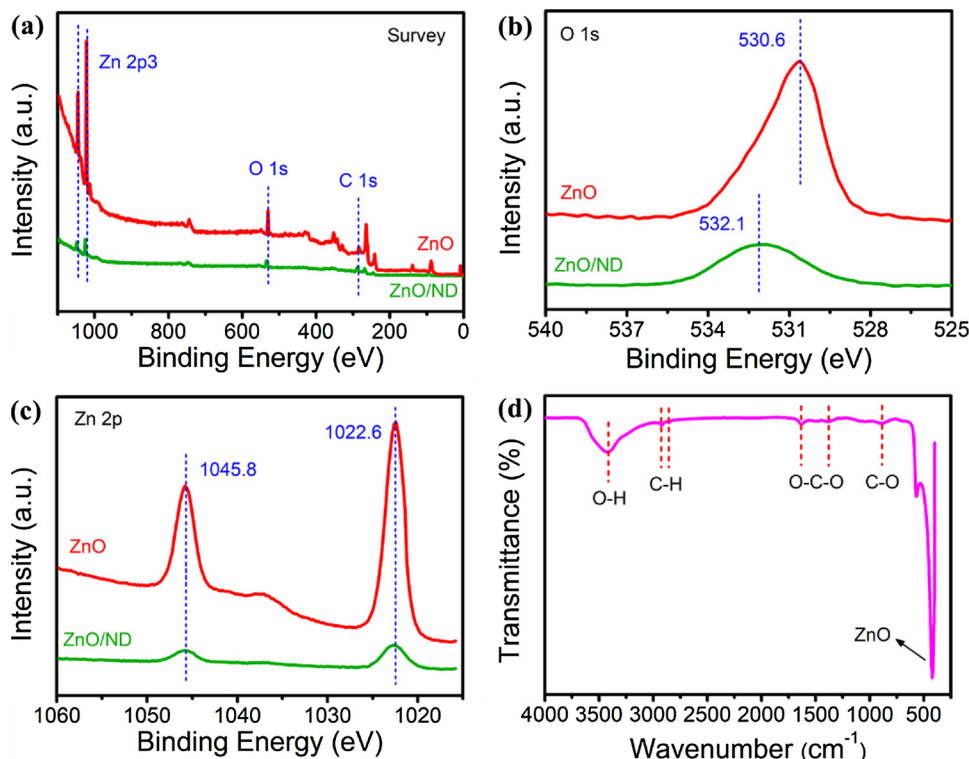


Fig. 7. XPS spectra of ZnO/ND: (a) survey, (b) O 1s and (c) Zn 2p; (d) FTIR spectrum of ZnO/ND.

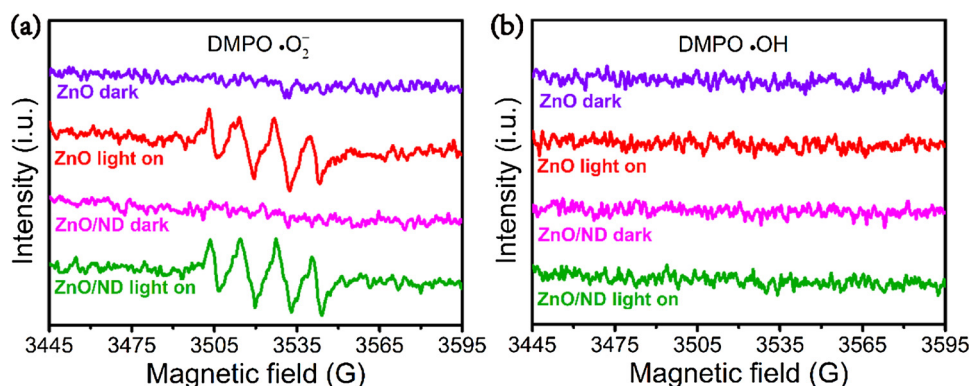


Fig. 8. EPR spectra of ZnO and ZnO/ND in the presence of DMPO as radical scavenger. The signals were collected under dark and UV-365 light irradiation, respectively. Conditions: sample concentration, 5 mg mL⁻¹; DMPO, 5 mM; irradiation time, 10 min; test temperature, 298 K.

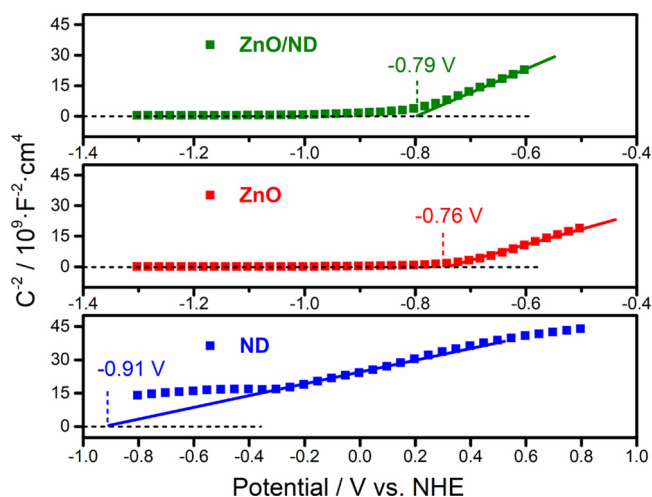


Fig. 9. Mott-Schottky plots of ND, ZnO and ZnO/ND.

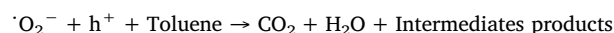
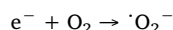
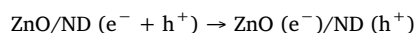
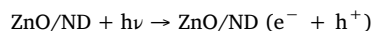
heterojunction was stretched by the decoration of ND. Whereas, since the band gap of ZnO/ND was slightly narrowed to 3.25 eV, the VB energy of that would also show a decline trend but not reached the highest valence band (VB) potential of ND, which was mainly resulted from that the content of ND added was much less than ZnO and the heterojunction still presented the properties of ZnO. Meanwhile, the presence of ND indeed promoted the charge transfer ability. Moreover, the CB potential of ZnO and ND were both more negative than the potential for the reduction of oxygen ($O_2 \rightarrow \cdot O_2^-$, -0.28 V vs. NHE) [55], suggesting that electrons on ZnO or ND could theoretically react with O_2 to form $\cdot O_2^-$. However, as the VB potential of ZnO or ND were both more negative than the potential for the oxidation of water ($H_2O \rightarrow \cdot OH$, 2.68 eV vs. NHE) [52], it could be concluded that they were not appropriate for the direct generation of $\cdot OH$ radicals from H_2O . In consequence, the EPR spectrum for DMPO- $\cdot O_2^-$ and DMPO- $\cdot OH$ demonstrated the massive production of $\cdot O_2^-$ and restriction of $\cdot OH$ generation on the ZnO/ND catalyst.

In situ DRIFTS studies were further carried out to infer the possible photooxidation process over the ZnO/ND. Fig. 10(a) showed the *in situ* DRIFTS spectra of the photooxidation of toluene on ZnO/ND. The bands around 1610 cm⁻¹ were assigned to the skeleton stretching vibrations of the aromatic ring, and the bands at 2340 and 2360 cm⁻¹ were assigned to CO_2 , the bands at 2870 and 2939 cm⁻¹ were correspond to the C-H stretching vibration of methyl, and the abroad absorption peaks from 3600 to 3800 cm⁻¹ were the feature bands of hydroxyl groups and acted as the main adsorption sites for toluene [56]. Fig. 10(b) showed the enlarged view of the bands located at 3600–3800 cm⁻¹. The bands at 3750, 3735, 3724 and 3712 cm⁻¹ were

correspond to the terminal hydroxyls, and the bands at 3688, 3676, 3649 and 3630 cm⁻¹ were correspond to the bridged -OH [57–59]. Fig. 10(c) showed the enlarged view of the bands located at 1400–1800 cm⁻¹. The bands at 1733 and 1685 cm⁻¹ were caused by the $\nu(C=O)$ mode of an aldehyde group and the vibrational mode of a carbonyl group, respectively. The bands at 1610, 1577 and 1508 cm⁻¹ were caused by the skeleton stretching vibrations of the aromatic ring [56]. Combining these two places, the formation of benzaldehyde could be inferred. The bands around 1558, 1541, and 1521 cm⁻¹ were attributed to the asymmetric stretching vibration of the carboxylate group COO^- , indicating the formation of benzoic acid [60,61]. The presence of oxalic acid with the bands at 1718, 1698 and 1418 cm⁻¹ for the $\nu(C=O)$, $\nu(C-O)$ and $\nu(C-C)$ of oxalic acid demonstrated the opening of the aromatic ring [62]. The band at 1636 cm⁻¹ was assigned to the bending mode of physically adsorbed water.

Fig. 10(d) showed the *in situ* DRIFTS spectra of the photooxidation of toluene on ZnO. It could be seen that the peaks at 1610 cm⁻¹ (the skeleton stretching vibrations of the aromatic ring) and 2939, 2870 cm⁻¹ (the C-H stretching vibration of methyl) were weak, indicating that the adsorption of toluene on ZnO was weak. The characteristic peaks of the intermediates generated at the range of 3800–3600 cm⁻¹ and 1800–1400 cm⁻¹ were also quite weak and shown in the Supplementary Information (Fig. S9).

Based on the above results, Fig. 11 presented the proposed mechanism of photocatalytic degradation of toluene upon ND-decorated ZnO photocatalysts. Both ZnO and ND could be excited to generate e^-/h^+ pairs under UV-365 light irradiation. After decorated with ND, free electrons of ND can transfer to ZnO to form a built-in electric field. Then the h^+ of ZnO transferred to ND to react with toluene rather than ZnO itself, thereby inhibiting the photocorrosion of ZnO effectively [63]. Meanwhile, the e^- of ND transferred to ZnO and reacted with O_2 molecules to form $\cdot O_2^-$ radicals, which was important and subsequently mineralized gaseous toluene and intermediates [64]. Because the VB edge potential of photocatalyst was more negative than the standard redox potential of $\cdot OH/H_2O$ pair, there was no $\cdot OH$ radicals generated during the process. Thus, the photo-generated h^+ might participated in the toluene oxidation reaction directly. The possible reactions of the photocatalytic process were described as follows [65]:



According to reports and the *in situ* DRIFTS results, the transformation from toluene to CO_2 included three processes [66]: (1) toluene reacted rapidly with $\cdot O_2^-$ species to generate benzaldehyde and benzoic acid gradually; (2) benzoic acid were then confirmed to be oxidized

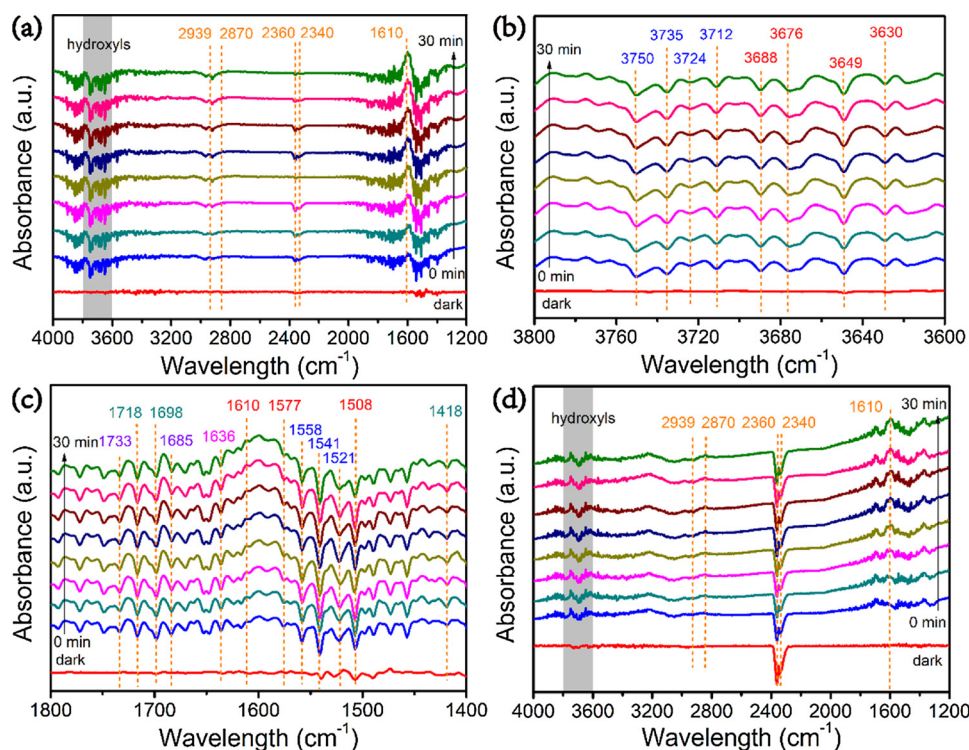


Fig. 10. (a) *In situ* DRIFTS spectra of toluene photo-oxidation on the ZnO/ND photocatalyst, (b) and (c) enlarged DRIFTS spectra at the wavenumber range of 3800–3600 cm^{-1} and 1800–1400 cm^{-1} from Fig. 8a, and (d) *in situ* DRIFTS spectra of toluene photo-oxidation on ZnO collected at dark, 0 min, 4 min, 8 min, 12 min, 16 min, 20 min, 24 min, 28 min and 30 min under UV-365 light irradiation.

rapidly to form oxalic acid that demonstrated the opening of the aromatic ring and decomposed into CO_2 and H_2O finally; (3) a part of benzaldehyde and benzoic acid might transfer into less-reactive intermediates, including benzene and hydroxylated intermediates (benzaldehyde, benzoic acid, etc.) that were much harder to mineralize to CO_2 . It was the reason why the degradation rate of toluene revealed a rapid increasing trend and then decreased gradually with the reaction time increased. Above all, the successful configuration of ZnO/ND heterojunction effectively increased the optical absorption and transient photocurrent, restrained the photo-generated electron-hole pairs recombination rate and electrochemical impedance, indicating that ND decoration not only improved the light adsorption for ZnO, but also promoted the charge transfer and eventually enhanced the photocatalytic oxidation efficiency of toluene as well as the photocorrosion resistance of ZnO. This work provides reasonable ways to design photocatalysts that suitable to toluene degradation and gives more possibility for the highly efficient indoor VOCs purification process.

4. Conclusion

In this work, the ND-decorated ZnO photocatalysts with heterostructure were designed reasonably by controlling the morphologies and exposed crystal planes of ZnO and tuning the surface treatment methods of ND, which effectively alleviated the photocorrosion problem of ZnO. The results showed that the bare ND decorated ZnO with higher amount of active (0001) crystal faced exposed performed the optimal photocatalytic efficiency of toluene oxidation, that was 50 ppm toluene could be completely removed in two hours under UV-365 light illumination. Either the thicker graphitic carbon layer of ND or more oxygen-containing functionality were not favored the photocatalytic activity. Furthermore, the moderate modification of ND could not only enhance the light absorption capacity, but also promoted the rapid separation of photogenerated carriers, thereby improving the photocatalytic ability to oxidize toluene as well as the photocorrosion resistance of ZnO. The active species that played a major role in the ND-decorated ZnO photocatalysts were superoxide radicals and photo-generated holes. The *in situ* DRIFTS results revealed that the decomposition pathways of toluene occurring as: toluene reacted with $\cdot\text{O}_2^-$

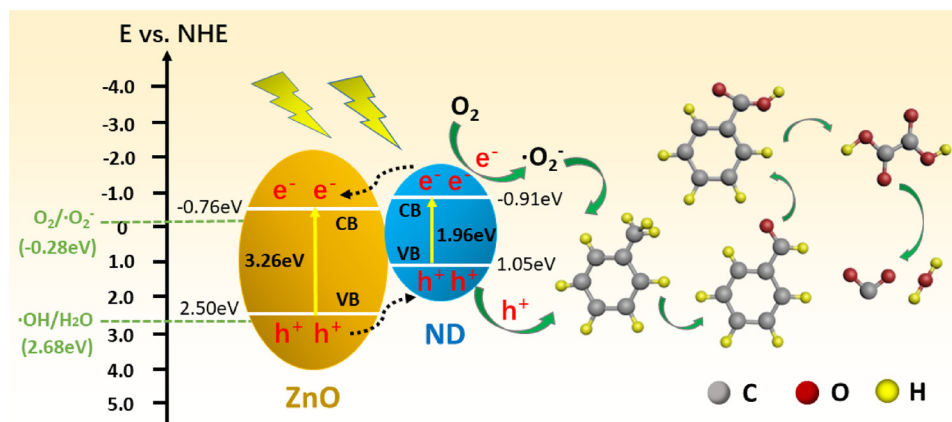


Fig. 11. Proposed mechanism for photocatalytic degradation of toluene upon ND-decorated ZnO photocatalysts.

species to generate benzaldehyde and benzoic acid gradually; benzoic acid was oxidized to from into oxalic acid and decomposed into CO₂ and H₂O finally. This work conducted herein could provide some new sights to relieve the photocorrosion problem of ZnO and also promote the photocatalytic efficiency for the removal of indoor volatile organic compounds by using non-noble metals modification.

Acknowledgement

The authors acknowledge the support of the National Natural Science Foundation of China (21722704), the Science and Technology Commission of Shanghai Municipality (17230741400 and 15DZ2281400) and the Shanghai Sailing Program (19YF1415300).

Appendix A. Supplementary data

Supplementary material related to this article can be found, in the online version, at doi:<https://doi.org/10.1016/j.apcatb.2019.117880>.

References

- [1] J. Gilman, B. Lerner, W. Kuster, J. Gouw, *Environ. Sci. Technol.* 47 (2013) 1297–1305.
- [2] C. Yang, G. Miao, Y. Pi, Q. Xia, J. Wu, Z. Li, J. Xiao, *Chem. Eng. J.* 370 (2019) 1128–1153.
- [3] J. Lemus, M. Martin-Martinez, J. Palomar, L. Gomez-Sainero, M. Gilarranz, J. Rodriguez, *Chem. Eng. J.* 211–212 (2012) 246–254.
- [4] Y. Yan, L. Wang, H. Zhang, *Chem. Eng. J.* 255 (2014) 195–204.
- [5] F. Thevenet, L. Sivachandiran, O. Guaitella, C. Barakat, A. Rousseau, *J. Phys. D Appl. Phys.* 47 (2014) 224011.
- [6] J. Chen, H. Zhang, P. Liu, Y. Li, X. Liu, G. Li, P. Wong, T. An, H. Zhao, *Appl. Catal. B: Environ.* 168–169 (2015) 266–273.
- [7] J. Chen, G. Li, Y. Huang, H. Zhang, H. Zhao, T. An, *Appl. Catal. B: Environ.* 123–124 (2012) 69–77.
- [8] J. Zheng, P. Liu, F. Huang, *Environ. Eng. Sci.* 32 (2015) 331–339.
- [9] H. Li, Z. Bian, J. Zhu, Y. Huo, H. Li, Y. Lu, *J. Am. Chem. Soc.* 129 (2007) 4538–4539.
- [10] H. Li, Z. Bian, J. Zhu, D. Zhang, G. Li, Y. Huo, Hui Li, Y. Lu, *J. Am. Chem. Soc.* 129 (2007) 8406–8407.
- [11] A. McLaren, T. Valdés-Solís, G. Li, S. Tsang, *J. Am. Chem. Soc.* 131 (2009) 12540–12541.
- [12] J. Chen, X. Wu, L. Yin, B. Li, X. Hong, Z. Fan, B. Chen, C. Xue, H. Zhang, *Angew. Chem. Int. Ed.* 54 (2015) 1210–1214.
- [13] R. Magudieswaran, J. Ishii, K. Raja, C. Terashima, R. Venkatachalam, A. Fujishima, S. Pitchaimuthu, *Mater. Lett.* 239 (2019) 40–44.
- [14] H. Yu, R. Shi, Y. Zhao, T. Bian, Y. Zhao, C. Zhou, G. Waterhouse, L. Wu, C. Tung, T. Zhang, *Adv. Mater.* 29 (2017).
- [15] F. Dong, Z. Wang, Y. Li, W. Ho, S. Lee, *Environ. Sci. Technol.* 48 (2014) 10345–10353.
- [16] Z. Wei, F. Liang, Y. Liu, W. Luo, J. Wang, W. Yao, Y. Zhu, *Appl. Catal. B: Environ.* 201 (2017) 600–606.
- [17] C. Pan, T. Takata, M. Nakabayashi, T. Matsumoto, N. Shibata, Y. Ikumura, K. Domen, *Angew. Chem. Int. Ed. Engl.* 54 (2015) 2955–2959.
- [18] D. Shi, R. Zheng, M.J. Sun, X. Cao, C.X. Sun, C.J. Cui, C.S. Liu, J. Zhao, M. Du, *Angew. Chem. Int. Ed.* 56 (2017) 14637–14641.
- [19] W. Fang, Z. Jiang, L. Yu, H. Liu, W. Shangguan, C. Terashima, A. Fujishima, *J. Catal.* 352 (2017) 155–159.
- [20] H. Huang, K. Xiao, Y. He, T. Zhang, F. Dong, X. Du, Y. Zhang, *Appl. Catal. B: Environ.* 199 (2016) 75–86.
- [21] Y. Zhu, Y. Wang, Q. Ling, Y. Zhu, *Appl. Catal. B: Environ.* 200 (2017) 222–229.
- [22] S. Weon, J. Choi, T. Park, W. Choi, *Appl. Catal. B: Environ.* 205 (2017) 386–392.
- [23] S. Weon, W. Choi, *Environ. Sci. Technol.* 50 (2016) 2556–2563.
- [24] H. Li, X. Zhang, Y. Huo, J. Zhu, *Environ. Sci. Technol.* 41 (2007) 4410–4414.
- [25] R. Kant, S. Pathak, V. Dutta, *Sol. Energy Mater. Sol. Cells* 178 (2018) 38–45.
- [26] H. Fu, T. Xu, S. Zhu, Y. Zhu, *Environ. Sci. Technol.* 42 (2008) 8064–8069.
- [27] T. Vu, L. del Río, T. Valdés-Solís, G. Marbán, *Appl. Catal. B: Environ.* 140–141 (2013) 189–198.
- [28] X. Ma, H. Li, T. Liu, S. Du, Q. Qiang, Y. Wang, S. Yin, T. Sato, *Appl. Catal. B: Environ.* 201 (2017) 348–358.
- [29] L. Yu, W. Chen, D. Li, J. Wang, Y. Shao, M. He, P. Wang, X. Zheng, *Appl. Catal. B: Environ.* 164 (2015) 453–461.
- [30] M. Zubair, A. Razzaq, C. Grimes, S. In, *J. CO₂ Util.* 20 (2017) 301–311.
- [31] Z. Dong, Y. Wu, N. Thirugnanam, G. Li, *Appl. Surf. Sci.* 430 (2018) 293–300.
- [32] W. Wang, N. Li, K. Hong, H. Guo, R. Ding, Z. Xia, *J. Alloys Compd.* 777 (2019) 1108–1114.
- [33] Z. Lin, J. Xiao, L. Li, P. Liu, C. Wang, G. Yang, *Adv. Energy Mater.* 6 (2016) 1501865.
- [34] K. Kim, N. Dey, H. Seo, Y. Kim, D. Lim, M. Lee, *Appl. Catal. A Gen.* 408 (2011) 148–155.
- [35] H. Kim, H. Kim, S. Weon, G. Moon, J. Kim, W. Choi, *ACS Catal.* 6 (2016) 8350–8360.
- [36] W. He, Y. Sun, G. Jiang, H. Huang, X. Zhang, F. Dong, *Appl. Catal. B: Environ.* 232 (2018) 340–347.
- [37] E. Jang, J. Won, S. Hwang, J. Choy, *Adv. Mater.* 18 (2006) 3309–3312.
- [38] M. Varga, T. Izak, V. Vretenar, H. Kozak, J. Holovsky, A. Artemenko, M. Hulman, V. Skakalova, D. Lee, A. Kromka, *Carbon* 111 (2017) 54–61.
- [39] A. Krüger, F. Kataoka, M. Ozawa, T. Fujino, Y. Suzuki, A. Aleksenskii, A. Vul', E. Osawa, *Carbon* 43 (2005) 1722–1730.
- [40] S. Michael, H. Huang, H. Feick, H. Yan, Y. Wu, H. Kind, E. Weber, R. Russo, P. Yang, *Science* 292 (2001) 1897–1900.
- [41] Z. Jiang, K. Zhu, Z. Lin, S. Jin, G. Li, *Rare Met.* 37 (2018) 881–885.
- [42] C. Zhang, J. Holoubek, X. Wu, A. Daniyar, L. Zhu, C. Chen, D. Leonard, I. Rodríguez-Pérez, J. Jiang, C. Fang, X. Ji, *Chem. Commun.* 54 (2018) 14097–14099.
- [43] J. Wang, L. Gao, *J. Cryst. Growth* 262 (2004) 290–294.
- [44] Y. Wang, L. Zhang, G. Wang, X. Peng, Z. Chu, C. Liang, *J. Cryst. Growth* 234 (2002) 171–175.
- [45] M. Shao, Q. Li, B. Xie, J. Wu, Y. Qian, *Mater. Chem. Phys.* 78 (2002) 288–291.
- [46] Y. Liu, C. Xie, J. Li, T. Zou, D. Zeng, *Appl. Catal. A Gen.* 433 (2012) 81–87.
- [47] H. Zhou, Z. Wen, J. Liu, J. Ke, X. Duan, S. Wang, *Appl. Catal. B: Environ.* 242 (2019) 76–84.
- [48] J. Mu, C. Shao, Z. Guo, Z. Zhang, M. Zhang, P. Zhang, B. Chen, Y. Liu, *ACS Appl. Mater. Interfaces* 3 (2011) 590–596.
- [49] W. Yu, D. Xu, T. Peng, *J. Mater. Chem. A* 3 (2015) 19936–19947.
- [50] H. Yu, H. Zhang, H. Huang, Y. Liu, H. Li, H. Ming, Z. Kang, *New J. Chem.* 36 (2012) 1031.
- [51] P. Wei, D. Qin, J. Chen, Y. Li, M. Wen, Y. Ji, G. Li, T. An, *Environ. Sci. Nano* 6 (2019) 959–969.
- [52] J. Wang, G. Wang, X. Wei, G. Liu, J. Li, *Appl. Surf. Sci.* 456 (2018) 666–675.
- [53] W. He, Y. Sun, G. Jiang, Y. Li, X. Zhang, Y. Zhang, Y. Zhou, F. Dong, *Appl. Catal. B: Environ.* 239 (2018) 619–627.
- [54] X. Gao, Y. Shang, L. Liu, F. Fu, *J. Catal.* 371 (2019) 71–80.
- [55] S. Gao, W. Cen, Q. Li, J. Li, Y. Lu, H. Wang, Z. Wu, *Appl. Catal. B: Environ.* 227 (2018) 190–197.
- [56] J. Liu, Y. Li, J. Ke, S. Wang, L. Wang, H. Xiao, *Appl. Catal. B: Environ.* 224 (2018) 705–714.
- [57] M. El-Roz, M. Kus, P. Cool, F. Thibault-Starzyk, *J. Phys. Chem. C* 116 (2012) 13252–13263.
- [58] A. Litke, Y. Su, I. Tranca, T. Weber, E. Hensen, J. Hofmann, *J. Phys. Chem. C Nanomater. Interfaces* 121 (2017) 7514–7524.
- [59] J. Sun, X. Li, Q. Zhao, M. Tade, S. Liu, *J. Mater. Chem. A* 3 (2015) 21655–21663.
- [60] M. Hernández-Alonso, I. Tejedor-Tejedor, J. Coronado, M. Anderson, *Appl. Catal. B: Environ.* 101 (2011) 283–293.
- [61] A. Mamaghani, F. Haghighat, C. Lee, *Appl. Catal. B: Environ.* 203 (2017) 247–269.
- [62] Y. Irokawa, T. Morikawa, K. Aoki, S. Kosaka, T. Ohwaki, Y. Taga, *Phys. Chem. Chem. Phys.* 8 (2006) 1116–1121.
- [63] Q. Xu, L. Zhang, J. Yu, S. Wageh, A. Al-Ghamdi, M. Jaroniec, *Mater. Today* 21 (2018) 1042–1063.
- [64] W. Zhang, G. Li, H. Liu, J. Chen, S. Ma, T. An, *Environ. Sci. Nano* 6 (2019) 948–958.
- [65] N. Li, Y. Tian, J. Zhao, J. Zhang, W. Zuo, L. Kong, H. Cui, *Chem. Eng. J.* 352 (2018) 412–422.
- [66] M. Sleiman, P. Conchon, C. Ferronato, J. Chovelon, *Appl. Catal. B: Environ.* 86 (2009) 159–165.